Impact of foreshock transients on the flank magnetopause and magnetosphere and the ionosphere

CHIH-PING WANG[1*], Xueyi Wang[2*], Terry Z. Liu[3, 4], Yu Lin[2]

[1]University of California, Los Angeles, United States, [2]Auburn University, United States, [3]University of Alaska Fairbanks, United States, [4]University Corporation for Atmospheric Research (UCAR), United States

Submitted to Journal:
Frontiers in Astronomy and Space Sciences

Specialty Section:
Space Physics

Article type:
Original Research Article

Manuscript ID:
751244

Received on:
31 Jul 2021

Revised on:
06 Sep 2021

Journal website link:
www.frontiersin.org

Conflict of interest statement

The authors declare that the research was conducted in the absence of any commercial or financial relationships that could be construed as a potential conflict of interest

Author contribution statement

Dr Chih-Ping Wang is responsible for analyzing the simulation results and the two observational events.
Dr Xueyi Wang and Prof Yu Lin are responsible for conducting the simulations and analysis of the simulation results.
Dr. Terry Liu is responsible for analyzing the two observational events.

Keywords

Keyword: Foreshock transients, Magnetosheath perturbations, Flank magnetopause distortion, compressional waves, field-aligned currents

Abstract

Word count: 229

Mesoscale (on the scales of a few minutes and a few RE) magnetosheath and magnetopause perturbations driven by foreshock transients have been observed in the flank magnetotail. In this paper, we present the 3D global hybrid simulation results to show qualitatively the 3D structure of the flank magnetopause distortion caused by foreshock transients and its impacts on the tail magnetosphere and the ionosphere. Foreshock transient perturbations consist of a low-density core and high-density edge(s), thus, after they propagate into the magnetosheath, they result in magnetosheath pressure perturbations that distort magnetopause. The magnetopause is distorted locally outward (inward) in response to the dip (peak) of the magnetosheath pressure perturbations. As the magnetosheath perturbations propagate tailward, they continue to distort the flank magnetopause. This qualitative explains the transient appearance of the magnetosphere observed in the flank magnetosheath associated with foreshock transients. The 3D structure of the magnetosheath perturbations and the shape of the distorted magnetopause keep evolving as they propagate tailward. The transient distortion of the magnetopause generates compressional magnetic field perturbations within the magnetosphere. The magnetopause distortion also alters currents around the magnetopause, generating field-aligned currents (FACs) flowing in and out of the ionosphere. As the magnetopause distortion propagates tailward, it results in localized enhancements of FACs in the ionosphere that propagate anti-sunward. This qualitatively explains the observed anti-sunward propagation of the ground magnetic field perturbations associated with foreshock transients.

Contribution to the field

Our current understanding of the impact of foreshock transients on the magnetosphere has been limited to the dayside. The open questions are how the magnetosheath perturbations associated with foreshock transients may evolve on the nightside and what are the 3D structure of the magnetosheath perturbations and the corresponding magnetopause distortion. This paper provides a 3D view of the impact on the nightside magnetopause and magnetosphere by foreshock transient-driven magnetosheath perturbations. This paper presents the first simulation investigation of the impact of the foreshock transients on the field-aligned currents on the nightside.". Our simulation results provide qualitative explanation of the mesoscale perturbations observed in the flank magnetosheath and the ionosphere

Funding statement

C.-P. Wang is supported by NASA 80NSSC19K0840. Xueyi Wang and Yu Lin are supported by NASA 80NSSC19K0840, 80NSSC17K0012, NNX17AI47G, and 80NSSC20K0604. T. Z. L. is supported by the NASA Living With a Star Jack Eddy Postdoctoral Fellowship Program, administered by the Cooperative Programs for the Advancement of Earth System Science (CPAESS). T. Z. L. is partially supported by NSF award AGS-1941012.

Ethics statements

Studies involving animal subjects
Generated Statement: No animal studies are presented in this manuscript.

Studies involving human subjects
Generated Statement: No human studies are presented in this manuscript.

Inclusion of identifiable human data
Generated Statement: No potentially identifiable human images or data is presented in this study.

Data availability statement

Generated Statement: The datasets presented in this study can be found in online repositories. The names of the repository/ repositories and accession number(s) can be found below: **https://doi.org/10.6084/m9.figshare.14058359.v1**.

Impact of foreshock transients on the flank magnetopause and magnetosphere and the ionosphere

Chih-Ping Wang[1], Xueyi Wang[2], Terry Z. Liu[3,4], Yu Lin[2]

1. Department of Atmospheric and Oceanic Sciences, University of California, Los Angeles, Los Angeles, CA, USA
2. Physics Department, Auburn University, Auburn, AL, USA
3. Cooperative Programs for the Advancement of Earth System Science, University Corporation for Atmospheric Research, Boulder, CO, USA
4. Geophysical Institute, University of Alaska, Fairbanks, Fairbanks, AK, USA.

Corresponding authors: Chih-Ping Wang (cat@atmos.ucla.edu) and Xueyi Wang (wangxu@auburn.edu)

Keyword: Foreshock transients, Magnetosheath perturbations, Flank magnetopause distortion, Compressional waves, Field-aligned currents

Abstract. Mesoscale (on the scales of a few minutes and a few R_E) magnetosheath and magnetopause perturbations driven by foreshock transients have been observed in the flank magnetotail. In this paper, we present the 3D global hybrid simulation results to show qualitatively the 3D structure of the flank magnetopause distortion caused by foreshock transients and its impacts on the tail magnetosphere and the ionosphere. Foreshock transient perturbations consist of a low-density core and high-density edge(s), thus, after they propagate into the magnetosheath, they result in magnetosheath pressure perturbations that distort magnetopause. The magnetopause is distorted locally outward (inward) in response to the dip (peak) of the magnetosheath pressure perturbations. As the magnetosheath perturbations propagate tailward, they continue to distort the flank magnetopause. This qualitatively explains the transient appearance of the magnetosphere observed in the flank magnetosheath associated with foreshock transients. The 3D structure of the magnetosheath perturbations and the shape of the distorted magnetopause keep evolving as they propagate tailward. The transient distortion of the magnetopause generates compressional magnetic field perturbations within the magnetosphere. The magnetopause distortion also alters currents around the magnetopause, generating field-aligned currents (FACs) flowing in and out of the ionosphere. As the magnetopause distortion propagates tailward, it results in localized enhancements of FACs in the ionosphere that propagate anti-sunward. This qualitatively explains the observed anti-sunward propagation of the ground magnetic field perturbations associated with foreshock transients.

1. Introduction

Perturbations in front of the bow shock are more frequently observed in front of the quasi-parallel shock (the foreshock) and the perturbed region extends further upstream, as compared to those in front of the quasi-perpendicular shock. In this paper, the mesoscale perturbations

generated in the foreshock are referred to as ion foreshock transients. There are many different types of foreshock transients with their time scales ranging from seconds to minutes and spatial scales ranging from foreshock ion gyroradius up to 10 R_E (Zhang and Zong, 2020). Almost all foreshock transient perturbations include a core with the number density and magnetic field strength lower than the background solar wind values and compression edge(s) with the density and magnetic field strength higher than the solar wind values. Some foreshock transients may also include flow deflection. Some foreshock transients are generated by the kinetic interaction of energetic ions reflected from the bow shock with interplanetary magnetic field (IMF) discontinuities, such as foreshock bubbles (Liu et al., 2015; 2016; Omidi et al., 2010; Omidi et al., 2020; Turner et al., 2013; Turner et al., 2020), hot flow anomalies (Chu et al., 2017; Lin, 1997; 2002; Liu et al., 2017; Lucek et al., 2004; Omidi and Sibeck, 2007; Schwartz et al., 1985; 2018; Thomsen et al., 1986; Zhang et al., 2010; 2017;), foreshock cavities (e.g., Billingham et al., 2008; Schwartz et al., 2006; Sibeck et al., 2002; 2004), and traveling foreshock (e.g., Kajdič et al., 2017), while some are formed without IMF discontinuities, such as diamagnetic cavities (Lin, 2003; Lin and Wang, 2005), foreshock cavitons (Blanco-Cano et al., 2011; Kajdič et al., 2013; Omidi, 2007), and spontaneous hot flow anomalies (Omidi et al., 2013; Zhang et al., 2013). The foreshock transients that do not have the density core are foreshock compressional boundary (e.g. Sibeck et al., 2008) and short large-amplitude magnetic structures (e.g., Schwartz, 1991). Some of the above transients, such as HFAs, can also be generated in front the quasi-perpendicular shock. Recent MHD simulations found that the bow shock response to transient density depleted regions in the solar wind can also result in structures that resemble HFAs (Otto and Zhang, 2021).

The density perturbations of foreshock transients result in perturbations in dynamic pressure. As the perturbations propagate into the magnetosheath, they can cause magnetopause distortion.

63 The resulting magnetosheath perturbations and the impact on the dayside magnetopause have been
64 simulated (e.g., Lin and Wang, 2005; Omidi et al., 2016; Sibeck et al., 2021)) and observed (e.g.,
65 Archer et al., 2014; 2015; Jacobsen et al., 2009; Kajdičet al., 2021; Sibeck et al., 1999; 2000).
66 Similar to the impact of the solar wind dynamic pressure perturbations, the magnetopause
67 distortion driven by foreshock transients can subsequently generate ultralow frequency (ULF)
68 waves inside the magnetosphere (e.g., Hartinger et al., 2013; Wang et al., 2017; Wang B. et al.,
69 2018b; 2019; 2020; 2021; Shi et al., 2021), enhance particle precipitation and the resulting aurora
70 brightness (e.g., Fillingim et al., 2011; Wang B. et al., 2018a; 2018b; 2019), and enhance field-
71 aligned currents (FACs) and the associated perturbations in ionospheric currents and ground
72 magnetic field (e.g., Fillingim et al., 2011; Ratac ka et al., 2002, Murr and Hughes, 2003; Shen et
73 al., 2018).
74 Recent studies have extended our understanding of the foreshock transients to the nightside. In
75 observations, Liu et al. (2020; 2021) reported foreshock transients observed in the midtail
76 foreshock around X ~ − 40 R_E. Using multi-point satellite measurements, Wang C. et al. (2018)
77 showed that the perturbations driven by foreshock transients can propagate tailward within the
78 flank magnetosheath to the midtail around X ~ − 50 R_E and can cause transient flank
79 magnetopause distortion. 3D global hybrid simulations have been conducted to investigate
80 foreshock transients associated with an IMF directional rotational discontinuity (RD) (Wang C. et
81 al., 2020) and tangential discontinuity (TD) (Wang C. et al., 2021). They showed the evolution of
82 the foreshock transient perturbations as they propagate from the dayside to nightside foreshock
83 and the associated magnetosheath perturbations in the flanks. In this paper, we use the simulation
84 by Wang et al. (2021) to show qualitatively the 3D structure of the flank magnetopause distortion
85 caused by foreshock transients and the impact on the magnetosphere and ionosphere. The results

86 presented here should provide a qualitative understanding of the impacts common to the foreshock
87 transients of different types since they all have the same features of density perturbations (low-
88 density core and high-density edge). We also present two observation events to provide qualitative
89 comparisons with the simulated magnetopause distortion and ionospheric perturbations.

90 **2. Simulation**

91 Wang et al. (2021) used the AuburN Global hybrId CodE in 3D (ANGIE3D) hybrid code (Lin
92 et al., 2014) to simulate foreshock transients resulting from the interaction of an IMF directional
93 TD (i.e., with direction change only) with the foreshock ions. The simulation model and setup for
94 this simulation is described in Section 2.1. In Sections 2.2 to 2.7, we present the simulation results
95 for the tailward propagating magnetosheath perturbations, the magnetopause distortion on the
96 dayside and the flanks, and the impacts on the magnetosphere and the ionosphere.

97 **2.1. Simulation Model and Setup**

98 In the ANGIE3D code, the ions (protons) are treated as discrete, fully kinetic particles, and the
99 electrons are treated as a massless fluid. Quasi charge neutrality is assumed. Detailed descriptions
100 of the equations for ion particle motion, electric and magnetic fields and assumptions used in the
101 ANGIE3D code are given in Lin et al. (2014). The code is valid for low-frequency physics with ω
102 $\sim\Omega_i$ and $k\rho_i \sim 1$ (wavelength $\lambda \sim 6\rho_i$), where ω is the wave frequency, k is the wave number, Ω_i is
103 the ion gyrofrequency, and ρ_i is the ion Larmor radius.

104 The simulation domain is $25 \geq X \geq -60$, $60 \geq Y \geq -35$, $35 \geq Z \geq -45$ R_E in the geocentric
105 solar magnetospheric (GSM) coordinates. Inflow time-dependent boundary conditions for the
106 solar wind are specified at the sunward boundary and open boundary conditions are used for the
107 rest of the outer boundaries. An inner boundary is assumed at the geocentric distance of $r \approx 3$ R_E.
108 This inner boundary is composed of a zigzag grid line approximating the spherical surface as in

109 global MHD simulations. For the region of the inner magnetosphere, a cold, incompressible ion
110 fluid is assumed to be dominant in $r < 6\ R_E$, which coexists with particle ions, since this simulation
111 focuses on the dynamics and ion kinetic physics in the outer magnetosphere. The inclusion of the
112 cold ion fluid in the inner magnetosphere simplifies the conditions for the fluid-dominant low-
113 altitude, inner boundary. A combination of spherical and Cartesian coordinates is used at the inner
114 boundary. We let particles be reflected at exactly $r = 3\ R_E$. This simple reflection of the ion parallel
115 velocity means that loss cone effects are omitted. The **E** and **B** fields at the boundary reside on the
116 Cartesian boundary approximating the spherical boundary, which are extrapolated to an extra grid
117 point inside the $r = 3\ R_E$ surface. The **B** field is assumed to maintain the dipole field values at the
118 inner boundary.

119 The ionospheric conditions (100 km altitude) are incorporated into the ANGIE3d code. The
120 FACs, calculated with the inner boundary, are mapped along the geomagnetic field lines into the
121 ionosphere as input to compute ionospheric potential. For this simulation, simplified ionospheric
122 conductance with uniform Pederson conductance of 10 siemens and Hall conductance of 5 siemens
123 is specified.

124 The TD is specified as a planar IMF discontinuity with a half-width of $0.12\ R_E$ and the normal
125 direction of (– 0.5, 0.86, 0). The TD propagates with a velocity of (– 400, 0, 33.7) km/s. At t = 0,
126 the TD plane intersects the Y = 0 axis at X = 185 R_E. Unless otherwise noted, downstream
127 (upstream) of the TD in this paper indicates the anti-sunward (sunward) side of the TD. The
128 downstream IMF direction is (3, 1.7, 0) nT and upstream IMF is (0, 0, – 3.4) nT. Constant solar
129 wind density of 5 cm^{-3} and isotropic solar wind ion temperature of 10 eV are used. The solar wind
130 velocities are (– 370.7, 16.8, 33.7) km/s downstream and (– 400, 0, 0) km/s upstream. The
131 average solar wind Alfvén Mach number is $M_A = 11.8$. These solar wind values are within the

typically observed ranges. To accomplish this large-scale simulation with the available computing resources and can still produce physical results, we choose the solar wind d_i to be 0.1 R_E (about 6 times larger than the realistic value) and the cell dimensions to be $n_x \times n_y \times n_z = 502 \times 507 \times 400$. Also, we use time-independent nonuniform cell sizes (ranging from ~0.1 to 0.5 R_E) so that we can appropriately assign cell sizes comparable to the d_i values in different key regions from the solar wind to the outer magnetosphere. The bow shock and magnetopause form self-consistently by the interaction of the solar wind with the geomagnetic dipole. Before the arrival of the TD, the bow shock nose is at X ~14 R_E and the magnetopause nose is at X ~10 R_E, similar to the realistic locations.

2.2. Magnetosheath Perturbations and Tailward Propagation

Figure 1a–1c show the 2D profiles of the magnetic field strength (|B|), ion density (N), and ion bulk flow speed (|v|), respectively, in the X-Y plane at Z = 0 at four different times from t = 53.4 to 75.3 min (see also Supplementary Movie 1 in Supplementary Material). The simulated magnetopause and bow shock are disturbed, so we also add in the t = 53.4 min plots two smooth model boundaries, the magnetopause locations predicted by Roelof and Sibeck (1993) and the bow shock locations predicted by Peredo et al. (1995), as visual references to help readers discern the magnetosheath perturbations. In this stimulation, before the arrival of the TD, the foreshock is mainly on the duskside extending from the dayside to the nightside. Note that there are weak perturbations in the foreshock and the magnetosheath due to the foreshock ULF waves. The TD first encounters the foreshock ions just outside the dayside bow shock at t ~44 min and foreshock transient perturbations are formed (see Wang et al. (2021) for more details about the initiation of the foreshock transient). The foreshock transient perturbations consist of a core with lower density, higher temperature, lower magnetic field strength, and lower anti-sunward bulk flow speed than

155 the values of the solar wind. An edge with relatively higher density and higher magnetic field
156 strength is on the upstream side of the core. As the TD (indicated by the black or white dashed
157 straight lines) propagates tailward, it continues to interact with the foreshock ions and generate
158 perturbations around the TD (the low-density core is indicted by magenta arrows in Figure 1b).
159 The perturbations newly generated just outside the bow shock subsequently enter the
160 magnetosheath via their anti-sunward flows and continue to propagate anti-sunward. Note that
161 these magnetosheath perturbations associated with the foreshock transients are the focus of this
162 paper, not the pre-existing perturbations associated with the foreshock ULF waves.
163 Figure 1 shows the tailward propagation of the magnetosheath plasma and magnetic field
164 perturbations resulting from foreshock transients. In the near-Earth region, as shown in the t = 53.4
165 and 59.7 min plots, the structures of magnetosheath perturbations are approximately aligned with
166 the TD plane (the black or white dashed line). The perturbations seen closer to the magnetopause
167 are associated with the foreshock transient perturbations that are generated and enter the
168 magnetosheath earlier, while those seen closer to the bow shock are associated with the foreshock
169 transient perturbations that are generated and enter the magnetosheath more recently. The newer
170 perturbations coming into the magnetosheath interact nonlinearly with those further inside, leading
171 to changes in the spatial structures of the perturbations across the magnetosheath. In this
172 simulation, the foreshock region extends to the nightside. Thus, as the TD propagates from the
173 near-Earth to the midtail, as shown in the t = 66 and 72.3 min plots, there are still new foreshock
174 transient perturbations being continuously added into the flank magnetosheath. As a result, the
175 magnetosheath perturbations are still strong in the midtail. Compared to the earlier magnetosheath
176 perturbations in the near-Earth flank shown in the t = 59.7 min plots, which are more spatially
177 confined around the TD plane and have well-defined structures, the spatial size of the mid-tail

178 magnetosheath perturbations shown in the t = 72.3 min plots have become larger and their spatial
179 structures become complex because of the nonlinear interaction described above.

180 **2.3. Dayside Magnetopause Distortion**

181 Figure 2 compares the dayside magnetosheath and magnetopause before the arrival of the TD
182 at t = 45.6 min with those associated with the magnetosheath perturbations at t = 52.8 min. As
183 shown in Figures 2a-2e for the X-Y distributions at Z = 0, at t = 45.6 min, there are small and
184 localized perturbations in both the magnetosheath plasma and the magnetopause shape (black or
185 white curves) associated with the foreshock ULF waves. The dayside magnetopause locations are
186 determined by tracing magnetic field lines from Z = 0 and the field lines in the dayside
187 magnetosphere are closed (both ends of the field lines are in the ionosphere). At t = 52.8 min, the
188 low-density core and high-density edge can be seen in the new perturbations forming outside the
189 bow shock as well as in the magnetosheath perturbations that have entered the magnetosheath
190 earlier (Figure 2b). The magnetic field strength is lower inside the core and higher at the edge
191 (Figure 2a). Figure 2c shows different flow speeds and directions for the core and edge, which
192 would later cause the spatial extents of the core and edge regions to change as they propagate
193 tailward. As a result of the lower density and flow speed within the core than at the edge, both the
194 thermal pressure (P_{th}) and the dynamic pressure along the direction normal to the magnetopause
195 ($P_{dyn,n}$) (the magnetopause normal direction in this paper is estimated using the model
196 magnetopause of Roelof and Sibeck (1993)) are relatively lower within the core and higher at the
197 edge. As shown in Figure 2d, the dayside magnetopause and magnetosphere intrude locally
198 outward for ~3 R_E into the magnetosheath in response to the lower P_n ($P_n = P_{th} + P_{dyn,n}$) of the core
199 and are distorted locally inward for ~1 R_E by the stronger P_n of the edge. The outward intruding
200 magnetosphere is indicated by the plasma with relatively higher magnetic field strength (Figure

2a) and lower density (Figure 2b) than the surrounding magnetosheath plasma. Figure 2e shows the perpendicular current density. It shows that the magnetosheath perturbations at t = 52.8 min results in strong perpendicular currents along the distorted magnetopause. Figures 2f-2g show the 2D X(Y)-Z profiles along the white dashed line indicated in Figure 2a (the TD plane at t = 52.8 min). The magnetopause outward distortion is seen mainly in the region of $|Z| < \sim 5\ R_E$ with the maximum distortion near Z = 0. The 1D profiles at Z = 0 along the white dashed line indicated in Figure 2a are shown in Figures 2h-2k. Comparing the 1D profiles between t = 45.6 and 52.8 min clearly show the changes in magnetic field components, flow velocity components, and pressure components outside the magnetopause (vertical magenta dashed lines) associated with the low-density core.

2.4. Flank Magnetopause Distortion

Figure 3 compares the X-Y distributions of the nightside magnetosheath and magnetosphere at Z = 0 at t = 45.6 with those at t = 60 min when the magnetosheath perturbations have propagated to the nightside around $X = -10\ R_E$. The magnetosheath perturbations at t = 60 min are seen to be around the TD line (white dashed line). Similar to the dayside magnetopause distortion shown in Figure 2, the magnetopause (indicated by white dashed line) intrudes locally outward into the magnetosheath around $X = -10\ R_E$ in response to the low-density core of the magnetosheath perturbations while it is distorted inward around $X = -7\ R_E$ in response to the high-density edge. In determining the nightside magnetopause boundaries shown in Figure 3 and later in Figures 4, 5, and 7, we investigate the magnetosonic Mach number from the magnetosheath to the magnetosphere and use the location of a quick drop in the Mach number values to below a certain threshold as the approximate location for the magnetopause boundary. The outward intruding magnetosphere can be seen by the plasma with relatively higher magnetic field strength (Figure

224 3a), lower density (Figure 3b), and higher temperature (Figure 3c) than the surrounding
225 magnetosheath plasma. Different from the slow-flowing plasma deep within the magnetosphere,
226 the intruding magnetospheric plasma has a strong tailward flow speed (Figure 3d). Figure 3e shows
227 the changes in the perpendicular current density within the magnetosphere associated with the
228 distorted magnetopause. This results in FACs flowing into and out of the ionosphere, as described
229 later in Section 2.6. Figure 3f shows the 3D view of the number density distributions at t = 60 min
230 from three different viewing angles together with the magnetic field lines. As indicated by the
231 closed magnetic field lines (red), the plasma sheet is seen within the outward intruding
232 magnetosphere. The field lines in the magnetosheath tailward of the intruding magnetosphere are
233 open field lines (purple, with one end connecting to the Earth) due to open flank magnetopause
234 resulting from the southward IMF downstream of the discontinuity, while those earthward of the
235 intruding magnetosphere are IMF field lines (light pink) corresponding to the southward IMF
236 upstream of the discontinuity.

237 The 3D structure of the outward intruding magnetosphere at t = 60 min shown in Figure 3 can
238 be better constructed with the 2D Y-Z and X-Z distributions cutting through the intrusion shown
239 in Figures 4a-4b and 4g-4h, respectively (see also Supplementary Movie 2 in Supplementary
240 Material). The magnetopause is distorted mainly in the region from Z ~ − 10 to 10 R_E with the
241 maximum outward distortion at Z ~0 (Figures 4a-4b) so that the cross-section in the X direction is
242 the widest near Z = 0 (Figures 4g-4h). The Y-profiles of plasma and magnetic field along the
243 cutting plane at Z = 0 are shown in Figures 4c-4f. As indicated by the vertical magenta dashed
244 line, the magnetopause boundary moves outward from Y ~18 to 24 R_E during the distortion.
245 Figures 4i-4m show the X-profiles at Z = 0 along Y = 21 R_E. The X scale of the intruding
246 magnetosphere is ~ 6 R_E.

Figures 5a-5c show the time sequence of the flank magnetopause (white solid curves) distortion in the X-Y, X-Z, and Y-Z planes, respectively. The white dotted curves in Figures 5a and 5c indicate the magnetopause at t = 45.6 min. Note that the magnetopause boundary shape can appear filamentary at some locations. This is associated with fine structures of the magnetosheath perturbations in the magnetic field strength and flow speed, which resulting in fine structures in the magnetosonic Mach number distributions used in determining the approximate magnetopause boundary. Figure 5 shows that as the magnetosheath perturbations move tailward from X ~ – 10 to X ~ – 40 R_E, they continue to distort the magnetopause. As described in section 2.1, the spatial structures of magnetosheath perturbations change substantially as they propagate tailward, thus the 3D structure of the outward intruding magnetosphere in the midtail (t = 70.4 min plot) is quite different from the earlier structure in the near-Earth tail (t = 60 min plot). The maximum outward intrusion remains around Z = 0 and it extends farther out in the Y direction with increasing downtail distances. The localized structure of the outward distortion shown in Figure 5 indicates that a satellite in the magnetosheath may observe the outward intruding magnetosphere with the probability strongly depending on the satellite locations.

Figure 6 shows the temporal profiles of magnetic field components, number density, ion temperature, and ion bulk flow velocities that would be observed by a virtual satellite in the magnetosheath at three downtail distances at Z ~0. Because of the passing of the localized outward magnetopause distortion, the virtual satellite would observe transient appearance of the magnetosphere, as indicated by the magnetic field strength, density, and temperature changing from the magnetosheath values to the magnetospheric values and then return to the magnetosheath values. These temporal profiles are qualitatively similar to the perturbations observed in the midtail magnetosheath at X = – 54 R_E reported by Wang C. et al. (2018). Another observation event in

the flank magnetosheath closer to the Earth is shown in Section 3.1.

2.5. Impact on the Magnetosphere

The localized and transient magnetopause distortion affects the magnetic field within the magnetosphere. Figure 7 shows a time sequence of the Y-Z distributions at X = – 10 R_E from the dusk flank to midnight for number density (Figure 7a), magnetic field strength (Figure 7b), amplitudes of the magnetic field perturbations in the parallel direction (Figure 7c), and perpendicular current strength (Figure 7d). The magnetic field perturbations shown in Figure 7c are obtained by subtracting the 10 min running averages. To better show the perturbations associated with waves propagating through a relatively uniform background, only the perturbations in the northern lobe where B_x > 15 nT are plotted in Figures 7c. As shown in the t = 45.6 min plot for before the arrival of the magnetopause distortion, there are weak magnetic field perturbations within the magnetosphere. These are due to the small magnetopause disturbances associated with the foreshock ULF waves, like that seen on the dayside as shown in Figure 2a for t = 45.6 min. As the magnetopause distortion passes through X = – 10 R_E, as shown in the t = 59.7 to t = 61.6 min plots in Figure 7, the magnetic field perturbations within the magnetosphere are enhanced. The enhancements are seen to extend from the dusk flank into the magnetosphere. Compared to the enhancements when the magnetopause is distorting outward around t ~60 min, the perturbations generated by the inward magnetopause distortion around t = 61.3 min are stronger and deeper into the magnetosphere. This shows that the magnetopause distortion driven by foreshock transients can launch compressional waves within the magnetosphere, which qualitatively explains the observed enhancements in magnetospheric ULF waves associated with foreshock transients (e.g., Hartinger et al., 2013; Wang et al., 2017; Wang B. et al., 2018b; 2019; 2020).

As shown in Figure 7b, the inward and outward motion of the distorted magnetopause alters the magnetospheric magnetic field near the flank in Y > ~10 R_E. This causes transient changes in the perpendicular currents in the flank magnetosphere shown Figure 7d as well as FACs flowing into or out of the ionosphere in order to maintain current continuity, establishing impact on the ionosphere. The resulting FAC perturbations in the ionosphere are shown in section 2.6.

2.6. Impact on the Ionosphere

Figures 8a and 8b show the FACs and FAC perturbations at t = 60 min, respectively, in the Northern Hemisphere (N.H.) ionosphere (positive value indicates FACs flowing into the N.H. ionosphere). The FAC perturbations are obtained by subtracting the 10-min averages of the FACs in the ionosphere. The FAC spatial distribution shown in Figure 8a has currents flowing into (out of) the ionosphere on the dawnside (duskside), which is the large-scale region-1 FACs connecting to the magnetosphere near the magnetopause. Figure 8b shows that the FAC perturbations are spatially localized. Figure 8c shows the time sequence of the ionospheric FAC perturbations in N.H. as a function of MLT and MLAT. Figure 8d shows the time series of N.H. FAC perturbations at different duskside MLT locations along MLAT = 73.5°. Figures 8c and 8d show that the region of enhanced FAC perturbations moves anti-sunward from near noon toward later MLTs, which is consistent with the tailward propagation of the flank magnetopause distortion. At t = 60 min, FAC perturbations have moved to nightside at ~18-20 MLT when the magnetopause distortion has propagated to nightside at X ~ – 10 R_E. The FAC perturbations would result in perturbations in the horizontal currents flowing in the ionosphere due to the current continuity, both would generate magnetic field perturbations on the ground.

Note that simplified and spatially uniform ionospheric conductance is used in this simulation and we do not further evaluate the simulated ionospheric horizontal currents. The spatial

316 distributions of the simulated ionospheric potential pattern and FACs corresponding to this
317 uniform conductance do not have day-night and dawn-dusk asymmetries as realistic as those
318 corresponding to non-uniform conductance that accounts for EUV and aurora contribution (Ridley
319 et al., 2014). We expect that using realistic EUV- and aurora-generated conductance would shift
320 the MLT and MLAT locations as well as the amplitudes of the perturbations in FAC and horizontal
321 currents, but it would not affect their physical connection with the flank magnetopause distortion
322 presented above. The simulated FAC perturbations seen at a fixed ionospheric location shown in
323 Figure 8d should still provide a qualitative explanation for the observed ground magnetic field
324 perturbations associated with foreshock transients (e.g., Shi et al., 2018). An observation event
325 for ground magnetic field perturbations propagating to the nightside is shown in Section 3.2.

326 **3. Observation Events**

327 In this section, we present two observation events associated with foreshock transients for
328 qualitative comparisons with the simulated flank magnetopause distortion and ionospheric
329 perturbations presented in section 2. The first event shows transient appearance of the
330 magnetosphere observed in the flank magnetosheath. The second event shows simultaneous
331 observations of the magnetosheath perturbations and ground magnetic field perturbations.

332 **3.1. An Event for Flank Magnetopause Distortion**

333 We present in Figure 9 an observation event for transient flank magnetopause distortion driven
334 by a foreshock transient on 31 May 2018. Figures 9a-9b show that Geotail was in the solar wind,
335 Cluster was in the dawnside magnetosheath at X ~ 0 (data from Cluster C4 probe are used), and
336 MMS was also in the dawnside magnetosheath further down the tail at X ~ – 18 R_E (data from
337 MMS-3 probe are used). Both Cluster and MMS were near Z = 0. Figures 9c-9d show that Geotail
338 observed two IMF directional discontinuities (no change in the IMF strength) at ~21:50 and 21:54

339 UT (indicated by the two vertical dashed lines), respectively. There were no changes in the solar
340 wind density (Figure 9d), temperature (Figure 9e), and flow speed (Figure 9f) across the
341 discontinuities. The IMF B_x was positive and IMF B_y was negative between the two
342 discontinuities. The same discontinuities were also observed earlier at ~21:05 UT by WIND at X
343 ~ 200 R_E (not shown) and the normal direction of the discontinuities estimated using the WIND-
344 Geotail pair is (–0.85, 0.12, 0.5). This IMF condition would result in a foreshock cavity on the
345 dawnside. The discontinuities later arrived at Cluster at ~22:05 UT (Figure 9g). The ~15 min delay
346 from Geotail to Cluster is expected from the propagation of the discontinuities being slowed down
347 after they entered the dayside magnetosheath (for example, see Figure 5 of Wang C. et al. (2020)
348 for the propagation of an RD in the magnetosheath). Between the discontinuities, Cluster observed
349 perturbations (yellow shaded region) with a core of low density (Figure 9h) and low magnetic field
350 strength (Figure 9g), slight flow deflection (a slight decrease in $|V_x|$ and increase in $|V_y|$) (Figure
351 9i), and some superthermal ions at ~ 10 keV (Figure 9j). An edge of slightly higher magnetic field
352 strength and density was seen next to the core (red shaded region at ~22:08 UT in Figures 9g and
353 9h). These confirm the magnetosheath perturbations associated with the expected foreshock
354 transient. Even though the type of the foreshock transient in this event is different from that of this
355 simulation, the observed magnetosheath perturbations are qualitatively similar to the simulated
356 perturbations shown in Figure 2 in the dayside magnetosheath. This is expected since, as described
357 in Introduction, almost all types of foreshock transients exhibit the same characteristics in their
358 density and magnetic field perturbations.

359 As the discontinuities and the magnetosheath perturbations observed at the Cluster location
360 moved to the MMS location at ~22:13 UT (Figure 9k), MMS observed transient appearance of the
361 magnetosphere (yellow shaded region). The magnetosphere is indicated by that the values for the

low density (Figure 9m) and high temperature (Figure 9n) within the yellow shaded region are typical for magnetospheric plasma. This change from the magnetosheath to the magnetosphere can also be seen in the sharp increases of ion fluxes at > 10 keV and decreases at < 2 keV shown in Figure 9p. This magnetospheric plasma seen intruding outward into the magnetosheath has substantial tailward flow speed, which is qualitatively consistent with the simulations shown in Figure 6b.

3.2. An Event for the Ionospheric Disturbances

We present in Figure 10 an observation event for ground magnetic field perturbations associated with a foreshock transient on 20 January 2010. This event has been reported by Wang C. et al. (2018) and they have shown simultaneous satellite observations of the event in the solar wind, foreshock, and flank magnetosheath. For this event, the driver discontinuity was observed by WIND in the solar wind. Geotail was on the dayside in the foreshock (the location is indicated in Figure 10a) and observed a transient low-density core with higher temperature and deflected flows (see Figure 4 of Wang C. et al. (2018) for the WIND and Geotail observations). The density perturbations observed by Geotail are shown in Figure 10a with the time of the discontinuity observed at the Geotail location indicated by the vertical magenta line. As shown in Figures 10b and 10c for P2 and P1, respectively, ARTEMIS P1 and P2 were both in the dawnside magnetosheath (their locations are indicated in the plots) with P2 closer to the Earth at X ~ − 27 R_E and P1 further down the tail at X ~ − 50 R_E. Figures 10a-10c show that the discontinuity and the associated low-density core observed at the Geotail location at 09:04 UT propagated to P2 at ~09:34 UT then to P1 at ~09:39 UT.

Figures 10d-10f show the ground magnetic field perturbations (obtained by subtracting the 10 min running averages) in the north-south direction observed by three magnetometer stations. The

three stations were on the dawnside at similar magnetic latitudes (~73°-76°) but at different MLTs from the dayside to the nightside (their MLTs and MLATs at 09:10 UT are indicated in the plots). The aurora image in N.H. from DMSP F17 satellite around 09:11 UT (not shown) indicates that the three stations were within diffuse aurora so that they were mapped to the closed field-line region of the magnetosphere. The ground magnetic field perturbations were enhanced at the three stations within the interval when the foreshock transient perturbations propagated from Geotail on the dayside to P2 and P1 on the nightside. The enhanced perturbations were first observed at ~11 MLT, then at 07 MLT, and then 04 MLT. These simultaneous observations of the tailward propagating magnetosheath perturbations and the anti-sunward propagating ground perturbations are qualitatively consistent with the simulated anti-sunward propagating FAC perturbations in the ionosphere shown in Figure 7 generated by the simulated tailward propagating magnetopause distortion shown in Figures 1-5.

4. Summary and Discussion

We use the 3D global hybrid simulation results of foreshock transient perturbations driven by a TD as an example to qualitatively describe the mesoscale (in a time scale of a few minutes and a spatial scale of a few R_E) distortion of the flank magnetopause resulting from the density/pressure perturbations of the foreshock transients. After the foreshock transient perturbations propagate into the magnetosheath, the low-density core contributes to a decrease of the magnetosheath pressure (thermal pressure and dynamic pressure), which causes the magnetopause to distort locally outward. On the other hand, the high-density edge results in an increase in the magnetosheath pressure and localized inward distortion of the magnetopause. The magnetosheath perturbations propagate tailward and continue to distort the flank magnetopause. This tailward-propagating localized outward distortion qualitatively explains the transient appearance of the magnetosphere

observed by satellites sitting in the flank magnetosheath. We show that the simulated flank magnetopause distortion can generate compressional magnetic field perturbations within the tail magnetosphere, which can explain the enhancements of magnetospheric ULF waves associated with foreshock transients reported in previous observation studies. As the magnetopause distortion propagates tailward, it generates FAC perturbations in the ionosphere propagating anti-sunward, which can qualitatively account for observed anti-sunward propagation of the ground magnetic field perturbations associated with the tailward propagating magnetosheath perturbations driven by foreshock transients.

The simulated magnetosheath perturbations and magnetopause distortion presented here are associated with foreshock transients generated by specific IMF and discontinuity conditions, nevertheless, we expect that they can provide a generalized and qualitative understanding of the transient and mesoscale nature of the impact on the nightside magnetopause/magnetosphere and the ionosphere since the density core and edge is the common feature to the majority of foreshock transients. In this simulation, |IMF B_y| is comparable to |IMF B_x| so that the foreshock region extends from the dayside to the nightside. Thus, as the TD propagates tailward to the nightside, it can still encounter foreshock ions so that new perturbations can be continuously generated and added into the magnetosheath. This process can be important to maintaining the significance of the magnetosheath perturbations and the corresponding flank magnetopause distortion as they propagate to the midtail. We expect that the nightside magnetosheath perturbations might become weaker in different scenarios when the IMF becomes more radial and the foreshock region is limited to the dayside. In that case, the foreshock transients entering the dayside magnetosheath would be the sole perturbations affecting the nightside magnetopause, and decay or diffuse of the perturbations during their tailward propagation would weaken their impact on the nightside. This

thought experiment will be further investigated in feature simulations.

Acknowledgment

C.-P. Wang is supported by NASA 80NSSC19K0840. Xueyi Wang and Yu Lin are supported by NASA 80NSSC19K0840, 80NSSC17K0012, NNX17AI47G, and 80NSSC20K0604. T. Z. L. is supported by the NASA Living With a Star Jack Eddy Postdoctoral Fellowship Program, administered by the Cooperative Programs for the Advancement of Earth System Science (CPAESS). T. Z. L. is partially supported by NSF award AGS-1941012. Computer resources for the simulations were provided by NASA Advanced Supercomputing (NAS) Division. The simulation data can be found at https://doi.org/10.6084/m9.figshare.14058659.v1.

References

Archer, M. O., D. L. Turner, J. P. Eastwood, T. S. Horbury, and S. J. Schwartz (2014), The role of pressure gradients in driving sunward magnetosheath flows and magnetopause motion, J. Geophys. Res. Space Physics, 119, 8117 – 8125, doi:10.1002/2014JA020342.

Archer, M. O., D. L. Turner, J. P. Eastwood, S. J. Schwartz, and T. S. Horbury (2015), Global impacts of a Foreshock Bubble: Magnetosheath, magnetopause and ground-based observations, Planet. Space Sci., 106, 56 – 65, doi:10.1016/j.pss.2014.11.026.

Billingham, L., Schwartz, S. J., & Sibeck, D. G. (2008). The statistics of foreshock cavities: Results of a Cluster survey. *Annales de Geophysique*, *26*, 3653 – 3667. https://doi.org/10.5194/angeo-26-3653-2008

Blanco-Cano, X., Kajdič , P., Omidi, N., and Russell, C. T. (2011), Foreshock cavitons for different interplanetary magnetic field geometries: Simulations and observations, J. Geophys. Res., 116, A09101, doi:10.1029/2010JA016413.

Chu, C., H. Zhang, D. Sibeck, A. Otto, Q. Zong, N. Omidi, J. P. McFadden, D. Fruehauff, and V.

Angelopoulos (2017), THEMIS satellite observations of hot flow anomalies at Earth's bow shock, Ann. Geophys., 35, 3, 443 – 451, doi:10.5194/angeo-35-443-2017.

Fillingim, M. O., J. P. Eastwood, G. K. Parks, V. Angelopoulos, I. R. Mann, S. B. Mende, *and* A. T. Weatherwax *(*2011*),* Polar UVI and THEMIS GMAG observations of the ionospheric response to a hot flow anomaly, J. Atmos. Sol. Terr. Phys., 73, 137 – 145, *doi:10.1016/j.jastp.2010.03.001.*

Hartinger, M. D., D. L. Turner, F. Plaschke, V. Angelopoulos, and H. Singer (2013), The role of transient ion foreshock phenomena in driving Pc5 ULF wave activity, J. Geophys. Res. Space Physics, 118, 299 – 312, doi:10.1029/2012JA018349.

Jacobsen, K. S., et al. (2009), THEMIS observations of extreme magnetopause motion caused by a hot flow anomaly, J. Geophys. Res., 114, A08210, doi:10.1029/2008JA013873.

Kajdič , P., X. Blanco-Cano, N. Omidi, K. Meziane, C. T. Russell, J.-A. Sauvaud, I. Dandouras, B. Lavraud (2013), Statistical study of foreshock cavitons, Annales Geophysicae, 10.5194/angeo-31-2163-2013, 31, 12, (2163-2178).

Kajdič, P., Blanco-Cano, X., Omidi, N., Rojas-Castillo, D., Sibeck, D. G., & Billingham, L. (2017). Traveling foreshocks and transient foreshock phenomena. *Journal Geophysical Research: Space Physics*, 122, 9148– 9168, https://doi.org/10.1002/2017JA023901

Kajdič, P., Raptis, S., Blanco-Cano, X., & Karlsson, T. (2021). Causes of jets in the quasi-perpendicular magnetosheath. *Geophysical Research Letters*, 48, e2021GL093173. https://doi.org/10.1029/2021GL093173

Kataoka, R., H. Fukunishi, L. J. Lanzerotti, T. J. Rosenberg, A. T. Weatherwax, M. J. Engebretson, and J. Watermann (2002), Traveling convection vortices induced by solar wind tangential discontinuities, J. Geophys. Res., 107(A12), 1455, doi:10.1029/2002JA009459.

Lin, Y. (1997). Generation of anomalous flows near the bow shock by its interaction with interplanetary discontinuities. Journal of Geophysical Research, 102, 24,265 – 24, 281.

Lin, Y. (2002), Global hybrid simulation of hot flow anomalies near the bow shock and in the magnetosheath, Planet. Space Sci., 50, 577.

Lin, Y. (2003), Global-scale simulation of foreshock structures at the quasi-parallel bow shock, J. Geophys. Res., 108, 1390, doi:10.1029/2003JA009991, A11.

Lin, Y., and X. Wang (2005), Three-dimensional global hybrid simulation of dayside dynamics associated with the quasi-parallel bow shock, J. Geophys. Res., 110, A12216, doi:10.1029/2005JA011243.

Lin, Y., X. Y. Wang, S. Lu, J. D. Perez, and Q. Lu (2014), Investigation of storm time magnetotail ion injection using three-dimensional global hybrid simulation, J. Geophys. Res. Space Physics, 119, doi:10.1002/2014JA020005.

Liu, Z., D. L. Turner, V. Angelopoulos, and N. Omidi (2015), THEMIS observations of tangential discontinuity-driven foreshock bubbles, Geophys. Res. Lett., 42, 7860 – 7866, doi:10.1002/2015GL065842.

Liu, T. Z., D. L. Turner, V. Angelopoulos, and N. Omidi (2016), Multipoint observations of the structure and evolution of foreshock bubbles and their relation to hot flow anomalies, J. Geophys. Res. Space Physics, 121, doi:10.1002/2016JA022461.

Liu, T. Z., V. Angelopoulos, H. Hietala, and L. B. Wilson III (2017), Statistical study of particle acceleration in the core of foreshock transients, J. Geophys. Res. Space Physics, 122, 7197 – 7208, doi:10.1002/2017JA024043.

Liu, T. Z., C.-P. Wang, Xueyi Wang, Hui Zhang, Yu Lin, and Vassilis Angelopoulos (2020), ARTEMIS observations of foreshock transients in the midtail foreshock. Geophys. Res.

Lett., 47, e2020GL090393. https://doi.org/10.1029/2020GL090393

Liu, J., Lyons, L. R., Wang, C.-P., Ma, Y., Strangeway, R. J., Zhang, Y., et al. (2021). Embedded Regions 1 and 2 field-aligned currents: Newly recognized from low-altitude spacecraft observations. *Journal of Geophysical Research: Space Physics*, 126, e2021JA029207. https://doi.org/10.1029/2021JA029207

Lucek, E. A., T. S. Horbury, A. Balogh, I. Dandouras, and H. Rème (2004), Cluster observations of hot flow anomalies, J. Geophys. Res., 109, A06207, doi:10.1029/2003JA010016.

Murr, D. L., and Hughes, W. J. (2003), Solar wind drivers of Traveling Convection Vortices, *Geophys. Res. Lett.*, 30, 1354, doi:10.1029/2002GL014987.

Omidi, N. (2007). Formation of cavities in the foreshock. AIP Conf. Proc. 932, 181.

Omidi, N. and D. Sibeck (2007), Formation of hot flow anomalies and solitary shocks, J. Geophys. Res., 112, A01203, doi:10.1029/2006JA011663.

Omidi, N., J. P. Eastwood, and D. G. Sibeck (2010), Foreshock bubbles and their global magnetospheric impacts, J. Geophys. Res., 115, A06204, doi:10.1029/2009JA014828.

Omidi, N., H. Zhang, D. Sibeck, and D. Turner (2013), Spontaneous hot flow anomalies at quasi-parallel shocks: 2. Hybrid simulations, J. Geophys. Res. Space Physics, 118, 173 – 180, doi: 10.1029/2012JA018099.

Omidi, N., J. Berchem, D. Sibeck, and H. Zhang (2016), Impacts of spontaneous hot flow anomalies on the magne- tosheath and magnetopause, J. Geophys. Res. Space Physics, 121, 3155 – 3169, doi:10.1002/ 2015JA022170.

Omidi, N., Lee, S. H., Sibeck, D. G., Turner, D. L., Liu, T. Z., & Angelopoulos, V. (2020). Formation and Topology of Foreshock Bubbles. Journal of Geophysical Research: Space Physics, 125, e2020JA028058. https://doi.org/10.1029/2020JA028058

Otto, A. and Zhang, H. (2021). Bow shock transients caused by solar wind dynamic pressure depletions, Journal of Atmospheric and Solar-Terrestrial Physics, Volume 218, 10.1016/j.jastp.2021.105615

Peredo, M., Slavin, J. A., Mazur, E., & Curtis, S. A. (1995). Three-dimensional position and shape of the bow shock and their variation with Alfvénic, sonic and magnetosonic Mach numbers and interplanetary magnetic field orientation. *Journal of Geophysical Research*, *100*(A5), 7907 – 7916. https://doi.org/10.1029/94JA02545

Ridley, A. J., Gombosi, T. I., & Dezeeuw, D. L. (2004). Ionospheric control of the magnetosphere: Conductance. Annales Geophysicae, 22(2), 567–584. https://doi.org/10.5194/angeo-22-567-2004

Roelof, E. C., & Sibeck, D. G. (1993). Magnetopause shape as a bivariate function of interplanetary magnetic field B_Z and solar wind dynamic pressure. *Journal of Geophysical Research*, *98*(A12), 21,421 – 21,450. https://doi.org/10.1029/93JA02362

Schwartz, S. J., et al. (1985), An active current sheet in the solar wind, Nature, 318, 269 – 271, doi:10.1038/318269a0.

Schwartz, S. J. (1991). Magnetic field structures and related phenomena at quasi-parallel shocks. *Adv. Space Res.*, *11*(9), 231.

Schwartz, S. J., Sibeck, D., Wilber, M., Meziane, K., & Horbury, T. S. (2006). Kinetic aspects of foreshock cavities. *Geophysical Research Letters*, *33*(12), 103. https://doi.org/10.1029/2005GL025612

Schwartz S. J., Avanov, L., Turner, D., Zhang, H., Gingell, I., Eastwood, J. P., et al. (2018). Ion kinetics in a hot flow anomaly: MMS observations. *Geophysical Research Letters*. 45, 11,520 – 11,529. https://doi.org/10.1029/2018GL080189

546 Shen, X.-C., Shi, Q., Wang, B., Zhang, H., Hudson, M. K., Nishimura, Y., et al. (2018). Dayside
547 magnetospheric and ionospheric responses to a foreshock transient on 25 June 2008: 1.
548 FLR observed by satellite and ground-based magnetometers. *Journal of Geophysical*
549 *Research: Space Physics*, *123*, 6335 – 6346. https://doi.org/10.1029/2018JA025349
550 Shi, F., Lin, Y., Wang, X., Wang, B., and Nishimura, Y. (2021). 3-D global hybrid simulations of
551 magnetospheric response to foreshock processes. Earth, Planes and Space, 73:138,
552 https://doi.org/10.1186/s40623-021-01469-2
553 Sibeck, D. G., Borodkova, N. L., Schwartz, S. J., Owen, C. J., Kessel, R., Kokubun, S., et al.
554 (1999). Comprehensive study of the magnetospheric response to a hot flow anomaly.
555 Journal of Geophysical Research, 104, 4577 – 4593.
556 Sibeck, D. G., et al. (2000). Magnetopause motion driven by interplanetary magnetic field
557 variations, *J. Geophys. Res.*, 105(A11), 25155– 25169, doi:10.1029/2000JA900109.
558 Sibeck, D. G., Phan, T.-D., Lin, R., Lepping, R. P., & Szabo, A. (2002). Wind observations of
559 foreshock cavities: A case study. *Journal of Geophysical Research*, *107*, 4 – 1. https://doi.
560 org/10.1029/2001JA007539
561 Sibeck, D. G., Kudela, K., Mukai, T., Nemecek, Z., & Safrankova, J. (2004). Radial dependence
562 of foreshock cav- ities: A case study. *Annales de Geophysique*, *22*, 4143 – 4151.
563 http://www.ann-geophys.net/22/4143/2004/
564 Sibeck, D. G., Omidi, N., Dandouras, I., & Lucek, E. (2008). On the edge of the foreshock: Model-
565 data comparisons. *Ann. Geophys.*, *26*, 1539–1544.
566 Sibeck, D. G., Lee, S.-H., Omidi, N., & Angelopoulos, V. (2021). Foreshock cavities: Direct
567 transmission through the bow shock. *Journal of Geophysical Research: Space Physics*,

126, e2021JA029201. https://doi.org/10.1029/2021JA029201

Thomsen, M. F., J. T. Gosling, S. A. Fuselier, S. J. Bame, and C. T. Russell (1986), Hot, diamagnetic cavities upstream from the Earth's bow shock, J. Geophys. Res., 91(A3), 2961 – 2973, doi:10.1029/JA091iA03p02961.

Turner, D. L., N. Omidi, D. G. Sibeck, and V. Angelopoulos (2013), First observations of foreshock bubbles upstream of Earth's bow shock: Characteristics and comparisons to HFAs, J. Geophys. Res. Space Physics, 118, 1552 – 1570, doi:10.1002/jgra.50198.

Turner, D. L., Liu, T. Z., Wilson, L. B., Cohen, I. J., Gershman, D. G., Fennell, J. F., et al. (2020). Microscopic, multipoint characterization of foreshock bubbles with Magnetospheric Multiscale (MMS). Journal of Geophysical Research: Space Physics, 125, e2019JA027707. https://doi.org/10.1029/2019JA027707

Wang, B., Nishimura, Y., Hietala, H., Lyons, L., Angelopoulos, V., Plaschke, F., et al. (2018a). Impacts of magnetosheath high-speed jets on the magnetosphere and ionosphere measured by optical imaging and satellite observations. Journal of Geophysical Research: Space Physics, 123, 4879 – 4894. https://doi.org/ 10.1029/2017JA024954

Wang, B., Nishimura, Y., Hietala, H., Shen, X.-C., Shi, Q., Zhang, H., et al. (2018b). Dayside magnetospheric and ionospheric responses to a foreshock transient on 25 June 2008: 2. 2-D evolution based on dayside auroral imaging. Journal of Geophysical Research: Space Physics, 123, 6347 – 6359. https://doi.org/10.1029/2017JA024846

Wang, B., Nishimura, Y., Zhang, H., Shen, X.-C., Lyons, L., Angelopoulos, V., et al (2019). The 2-D structure of foreshock-driven field line resonances observed by THEMIS satellite and ground-based imager conjunctions. Journal of Geophysical Research: Space Physics, 124,

6792 – 6811. https://doi. org/10.1029/2019JA026668

Wang, B., Liu, T., Nishimura, Y., Zhang, H., Hartinger, M., Shi, X., et al. (2020). Global propagation of magnetospheric Pc5 ULF waves driven by foreshock transients. Journal of Geophysical Research: Space Physics, 125, e2020JA028411. https://doi.org/ 10.1029/2020JA028411

Wang, B., Zhang, H., Liu, Z., Liu, T., Li, X., & Angelopoulos, V. (2021). Energy modulations of magnetospheric ions induced by foreshock transient-driven ultralow-frequency waves. Geophysical Research Letters, 48, e2021GL093913. https://doi.org/10.1029/2021GL093913

Wang, C.-P., et al. (2017), A multispacecraft event study of Pc5 ultralow-frequency waves in the magnetosphere and their external drivers, J. Geophys. Res. Space Physics, 122, doi:10.1002/2016JA023610.

Wang, C.-P., Liu, T. Z., Xing, X., & Masson, A. (2018). Multispacecraft observations of tailward propagation of transient foreshock perturbations to midtail magnetosheath. Journal of Geophysical Research: Space Physics, 123. https://doi.org/10.1029/2018JA025921

Wang, C.-P., Wang, X., Liu, T. Z., & Lin, Y. (2020). Evolution of a foreshock bubble in the midtail foreshock and impact on the magnetopause: 3-D global hybrid simulation. Geophysical Research Letters, 47, e2020GL089844. https://doi.org/10.1029/2020GL089844

Wang, C.-P., Wang, X., Liu, T. Z., & Lin, Y. (2021). A foreshock bubble driven by an IMF tangential discontinuity: 3D global hybrid simulation. *Geophysical Research Letters*, *48*, e2021GL093068. https://doi.org/10.1029/2021GL093068

Zhang, H., D. G. Sibeck, Q.-G. Zong, S. P. Gary, J. P. McFadden, D. Larson, K.-H. Glassmeier, and V. Angelopoulos (2010), Time History of Events and Macroscale Interactions during

Substorms observations of a series of hot flow anomaly events, J. Geophys. Res., 115, A12235, doi:10.1029/2009JA015180.

Zhang, H., D. G. Sibeck, Q.-G. Zong, N. Omidi, D. Turner, and L. B. N. Clausen (2013), Spontaneous hot flow anomalies at quasi-parallel shocks: 1. Observations, J. Geophys. Res. Space Physics, 118, 3357 – 3363, doi:10.1002/jgra.50376.

Zhang, H., G. Le, D. G. Sibeck (2017), MMS observations of a Hot Flow Anomaly in the magnetosheath, American Geophysical Union, Fall Meeting 2017, abstract #SM11B-230

Zhang, H. and Zong, Q. (2020). Transient Phenomena at the Magnetopause and Bow Shock and Their Ground Signatures. In Dayside Magnetosphere Interactions (eds Q. Zong, P. Escoubet, D. Sibeck, G. Le and H. Zhang). doi:10.1002/9781119509592.ch2

Figure Captions

Figure 1. Time sequences of the X-Y distributions from t = 53.4 to 72.3 min at Z = 0 for (a) magnetic field strength, (b) number density, and (c) ion bulk flow speed. The straight white or black dashed lines indicate the projection of the TD plane. The white curve in the top panel indicates the model magnetopause from Roelof and Sibeck (1993) and the black curve indicates the model bow shock from Peredo et al. (1995). The magenta arrows in (b) indicate the low-density core.

Figure 2. The X-Y distributions at Z = 0 for (a) magnetic field strength, (b) number density, (c) ion bulk flow speed and flow directions (black arrows), (d) pressure along the direction normal to the model magnetopause, (e) perpendicular current density at t = 45.6 (left panels) and 52.8 min (right panels). The straight white dashed lines indicate the projection of the TD plane at t = 52.8 min. The black or white curves in (a-g) indicate approximately the simulated magnetopause. The white dotted curves in (a) indicates the model magnetopause based on Roelof and Sibeck (1993).

(f-k) The 2-D and 1-D profiles at t = 45.6 (left) and 52.8 min (right) along the TD plane at t = 52.8 min indicated in (a): The 2-D profiles for (f) magnetic field strength and (g) number density. The 1-D profiles at Z = 0 for (h) magnetic field components, (i) number density, (j) ion bulk flow velocities, and (k) pressures. The magenta dashed line in (h)-(k) indicate approximately the magnetopause.

Figure 3. The X-Y distributions at Z = 0 for (a) magnetic field strength, (b) number density, (c) ion temperature, (d) ion bulk flow speed and flow directions (black arrows), and (e) perpendicular current density at t = 45.6 (left panels) and 60 min (right panels). The black or white curves indicate approximately the magnetopause boundary. The straight white dashed lines in the left panels indicate the projection of the TD plane at t = 60 min. (f) Number density distributions at t = 60 min viewing from three angles. The red curves indicate closed magnetic field lines, the orange lines indicate open magnetic field lines, and light pink lines indicate IMF field lines.

Figure 4. The Y-Z distributions at X = –10 R_E for (a) magnetic field strength and (b) number density and the Y profiles at X = –10 and Z = 0 R_E for (c) magnetic field components, (d) number density, (e) ion temperature, and (f) ion bulk flow velocities at t = 45.6 (left panels) and 60 min (right panels). The X-Z distributions at Y = 21 R_E for (g) magnetic field strength and (h) number density and the X profiles at Y = 21 and Z = 0 R_E for (i) magnetic field components, (j) number density, (k) ion temperature, and (m) ion bulk flow velocities at t = 45.6 (left panels) and 60 min (right panels). The white or black curves in (a-b) and (g-h) indicate approximately the magnetopause boundary. The vertical magenta dashed lines in (c-f) and (i-m) indicate the magnetopause.

Figure 5. Time sequences of number density distributions in (a) X-Y, (b) X-Z, and (c) Y-Z planes from t = 60 to 70.4 min. The white solid curves indicate approximately the magnetopause. The

660 white dotted curves in (a) and (c) indicate the magnetopause at t = 45.6 min. The straight white
661 dashed lines in (a) indicate the projection of the TD plane.
662 **Figure 6.** Temporal profiles at (a) X = 0, Y = 17, and Z = 0 R_E, (b) X = –20, Y = 22, and Z = 0
663 R_E, and (c) X = –40, Y = 28, and Z =1 R_E. From top to bottom: Magnetic field components, number
664 density, ion temperature, and ion bulk flow velocities.
665 **Figure 7.** Time sequences of the Y-Z profiles at X = –10 R_E from t = 45.6 to 66 min for (a) number
666 density, (b) magnetic field strength, and (c) the amplitudes of magnetic field perturbations in the
667 parallel direction in the northern lobe where B_x > 15 nT, and (d) perpendicular current density.
668 The black curves indicate approximately the magnetopause.
669 **Figure 8.** (a) FAC and (b) FAC perturbations at t = 60 min in the N.H. (c) Time sequences of the
670 MLAT-MLT distributions for the FAC perturbations in the ionosphere from t = 51.2 to 64.4 min.
671 (b) Time series of the FAC perturbations at different MLTs along MLAT = 73.5°.
672 **Figure 9.** A foreshock transient event on 31 May 2018. The projections of the locations of Geotail,
673 Cluster C4, and MMS-3 on (a) X-Y and (b) X-Z planes. Geotail observations of (c) magnetic field
674 components, (d) number density, (e) ion temperature, and (f) ion bulk flow velocities. The two
675 vertical dashed lines indicate the two discontinuities. Cluster observations of (g) magnetic field
676 components, (h) number density, (i) ion bulk flow velocities, and (j) ion energy flux (eV/(s-sr-cm^2-
677 eV)). The shaded yellow and red region indicate the core and edge of the magnetosheath
678 perturbations, respectively. MMS observations of (k) magnetic field components, (m) number
679 density, (n) ion temperature, (o) ion bulk flow velocities, and (p) ion energy fluxes (eV/(s-sr-cm^2-
680 eV)). The shaded yellow region indicates the magnetosphere.
681 **Figure 10.** A foreshock transient event on 20 January 2010. The number density observed by (a)
682 Geotail, (b) ARTEMIS P2, and (c) AREMIS P1. The vertical magenta line indicates the time when

683 the IMF discontinuity was observed. The ground magnetic field perturbations (perturbations from
684 10-min running averages) in the north-south direction observed at (d) HRN, (e) UMQ, and (f) CDC
685 stations.

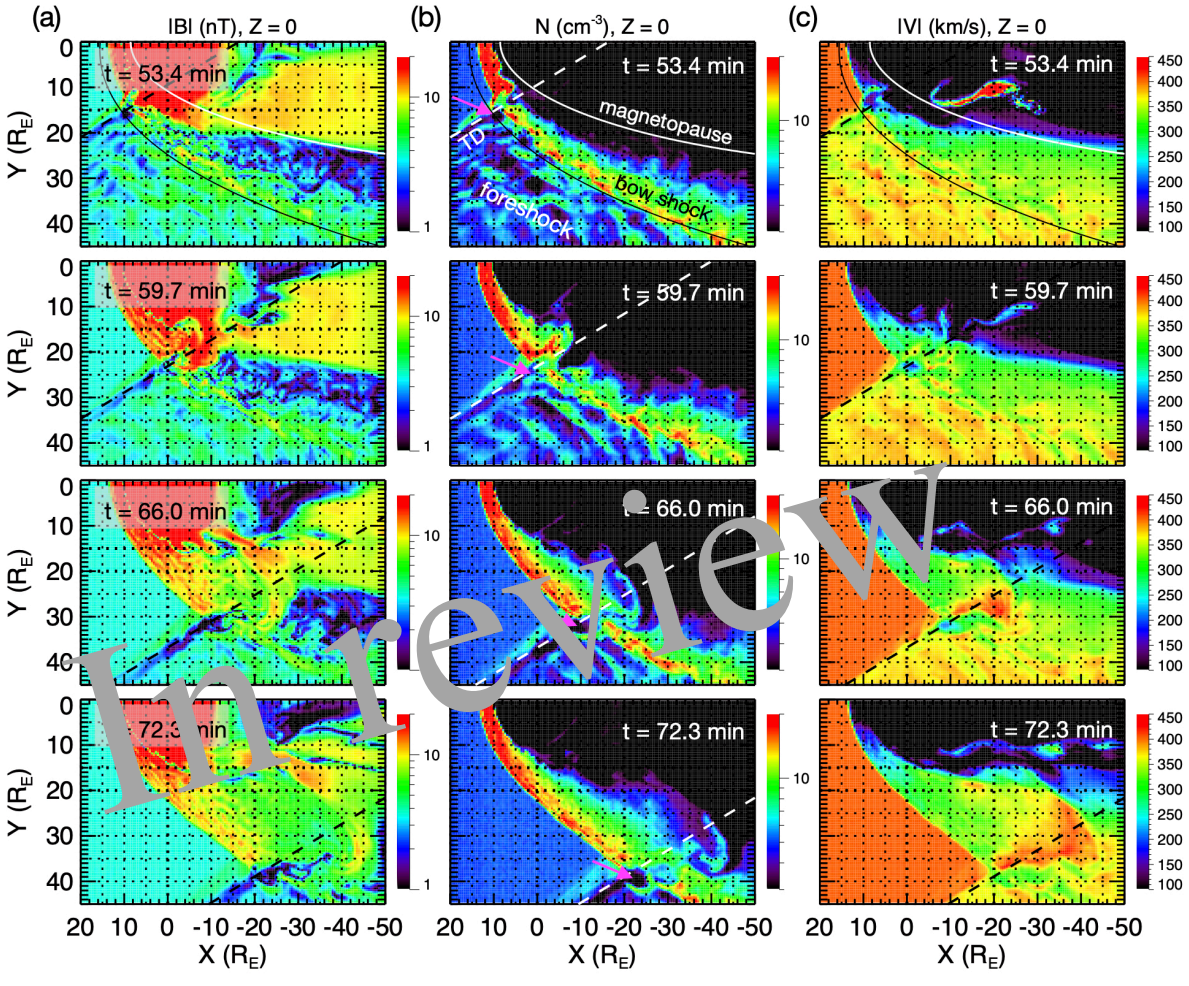

Figure 1. Time sequences of the X-Y distributions from t = 53.4 to 72.3 min at Z = 0 for (a) magnetic field strength, (b) number density, and (c) ion bulk flow speed. The straight white or black dashed lines indicate the projection of the TD plane. The white curve in the top panel indicates the model magnetopause from Roelof and Sibeck (1993) and the black curve indicates the model bow shock from Peredo et al. (1995). The magenta arrows in (b) indicate the low-density core.

Figure 2.JPEG

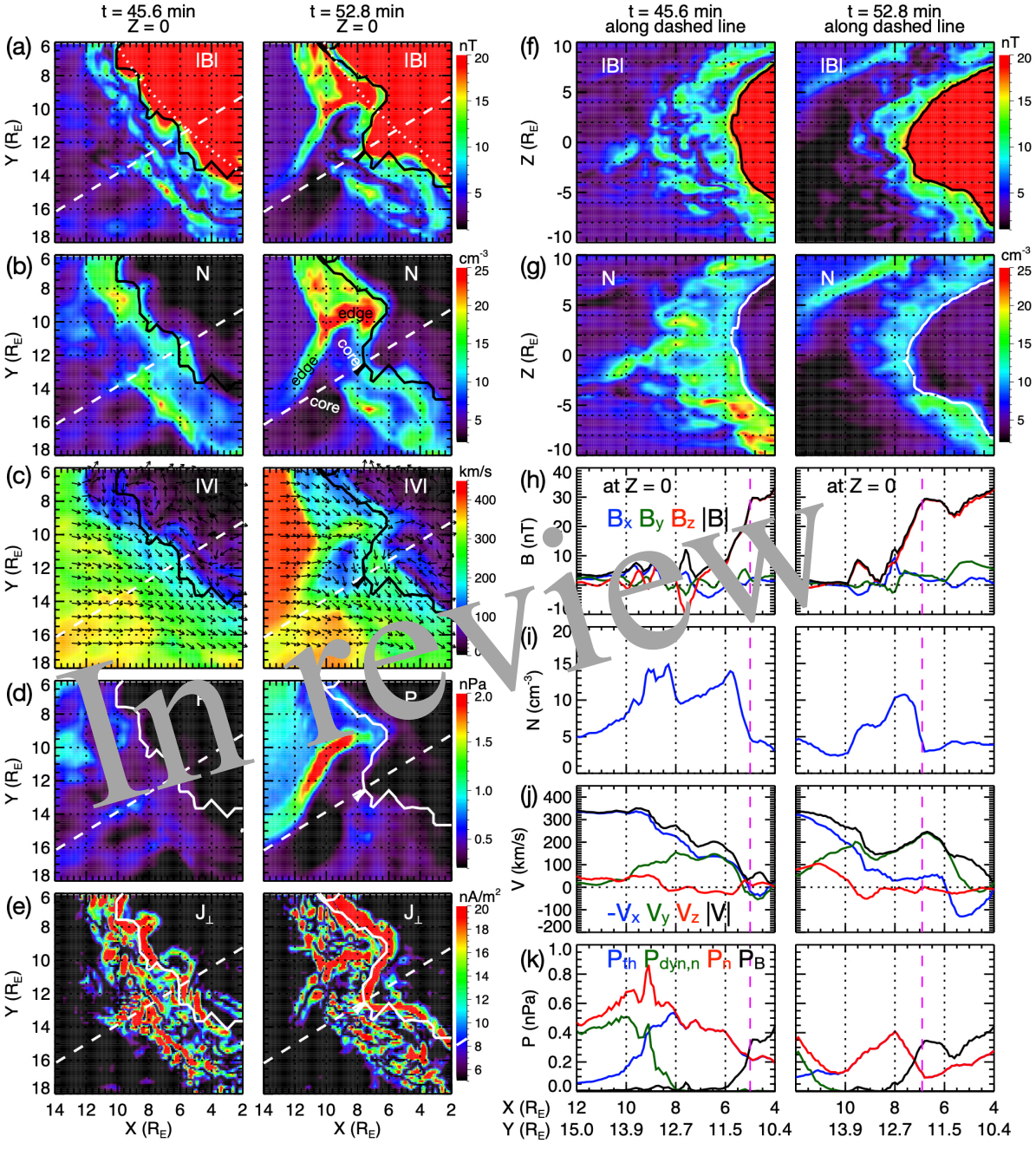

Figure 2. The X-Y distributions at Z = 0 for (a) magnetic field strength, (b) number density, (c) ion bulk flow speed and flow directions (black arrows), (d) pressure along the direction normal to the model magnetopause, (e) perpendicular current density at t = 45.6 (left panels) and 52.8 min (right panels). The straight white dashed lines indicate the projection of the TD plane at t = 52.8 min. The black or white curves in (a-g) indicate approximately the simulated magnetopause. The white dotted curves in (a) indicates the model magnetopause based on Roelof and Sibeck (1993). (f-k) The 2-D and 1-D profiles at t = 45.6 (left) and 52.8 min (right) along the TD plane at t = 52.8 min indicated in (a): The 2-D profiles for (f) magnetic field strength and (g) number density. The 1-D profiles at Z = 0 for (h) magnetic field components, (i) number density, (j) ion bulk flow velocities, and (k) pressures. The magenta dashed line in (h)-(k) indicate approximately the magnetopause.

Figure 3.JPEG

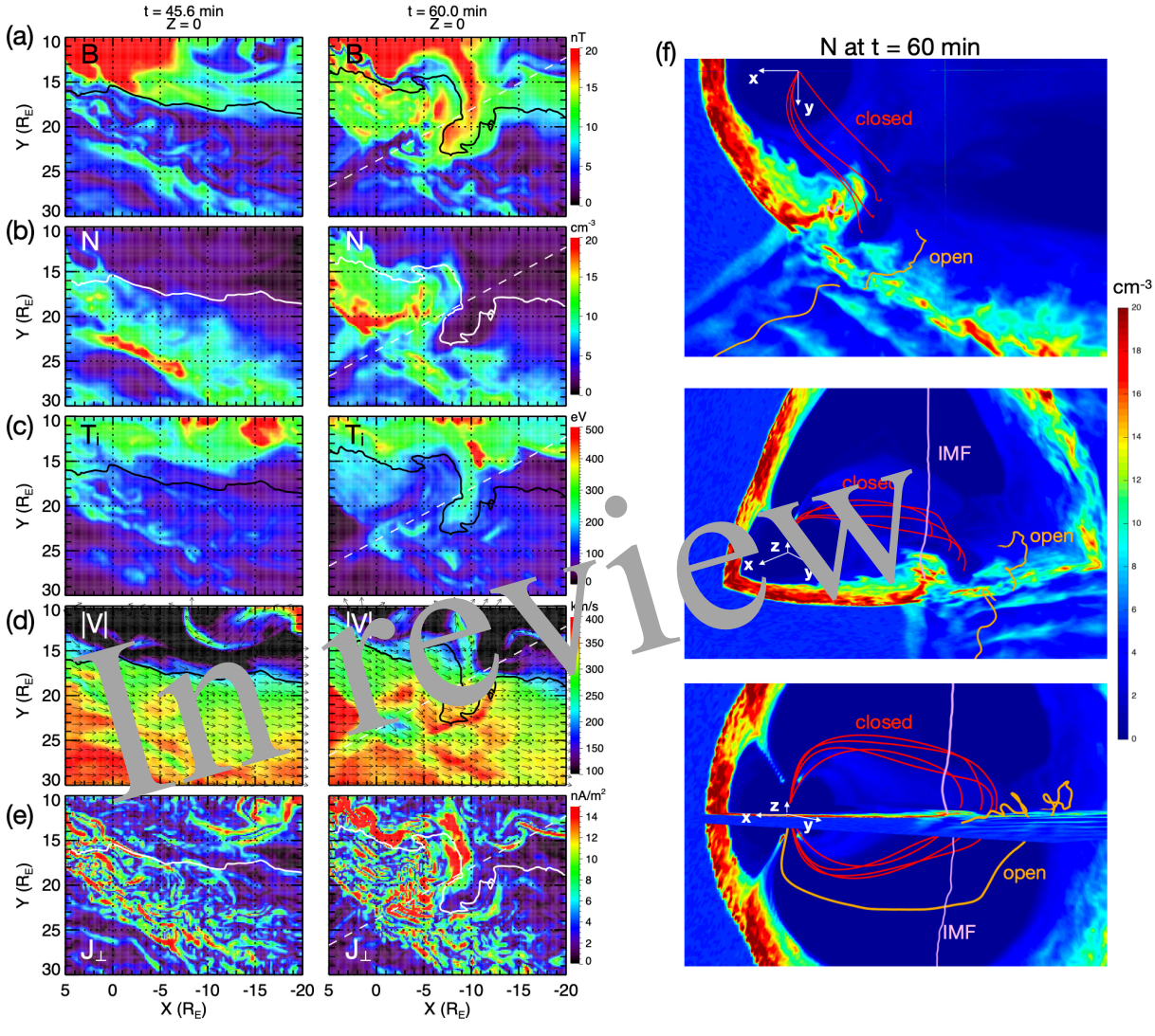

Figure 3. The X-Y distributions at Z = 0 for (a) magnetic field strength, (b) number density, (c) ion temperature, (d) ion bulk flow speed and flow directions (black arrows), and (e) perpendicular current density at t = 45.6 (left panels) and 60 min (right panels). The black or white curves indicate approximately the magnetopause boundary. The straight white dashed lines in the left panels indicate the projection of the TD plane at t = 60 min. (f) Number density distributions at t = 60 min viewing from three angles. The red curves indicate closed magnetic field lines, the orange lines indicate open magnetic field lines, and light pink lines indicate IMF field lines.

Figure 4.JPEG

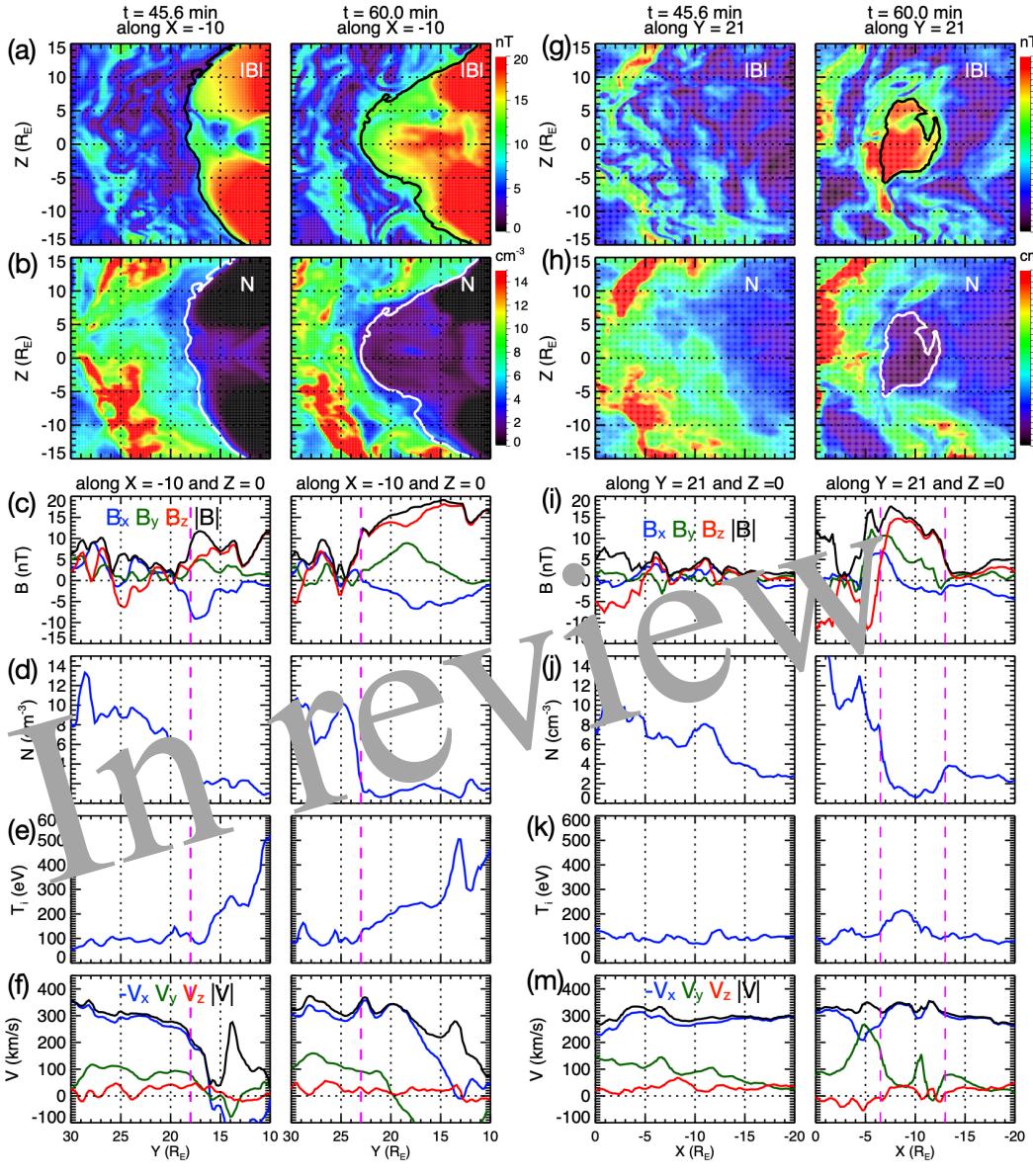

Figure 4. The Y-Z distributions at X = –10 R_E for (a) magnetic field strength and (b) number density and the Y profiles at X = –10 and Z = 0 R_E for (c) magnetic field components, (d) number density, (e) ion temperature, and (f) ion bulk flow velocities at t = 45.6 (left panels) and 60 min (right panels). The X-Z distributions at Y = 21 R_E for (g) magnetic field strength and (h) number density and the X profiles at Y = 21 and Z = 0 R_E for (i) magnetic field components, (j) number density, (k) ion temperature, and (m) ion bulk flow velocities at t = 45.6 (left panels) and 60 min (right panels). The white or black curves in (a-b) and (g-h) indicate approximately the magnetopause boundary. The vertical magenta dashed lines in (c-f) and (i-m) indicate the magnetopause.

Figure 5.JPEG

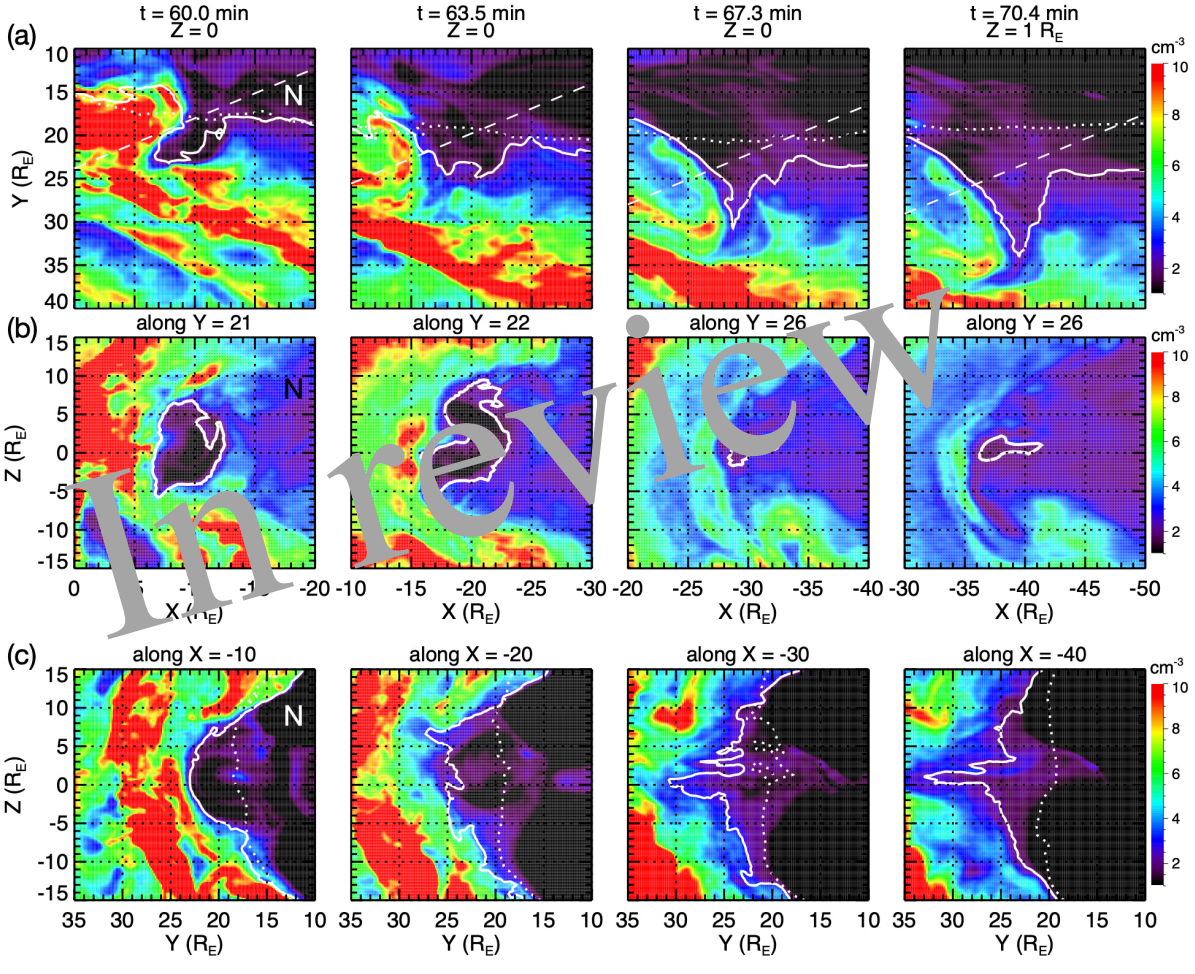

Figure 5. Time sequences of number density distributions in (a) X-Y, (b) X-Z, and (c) Y-Z planes from t = 60 to 70.4 min. The white solid curves indicate approximately the magnetopause. The white dotted curves in (a) and (c) indicate the magnetopause at t = 45.6 min. The straight white dashed lines in (a) indicate the projection of the TD plane.

Figure 6.JPEG

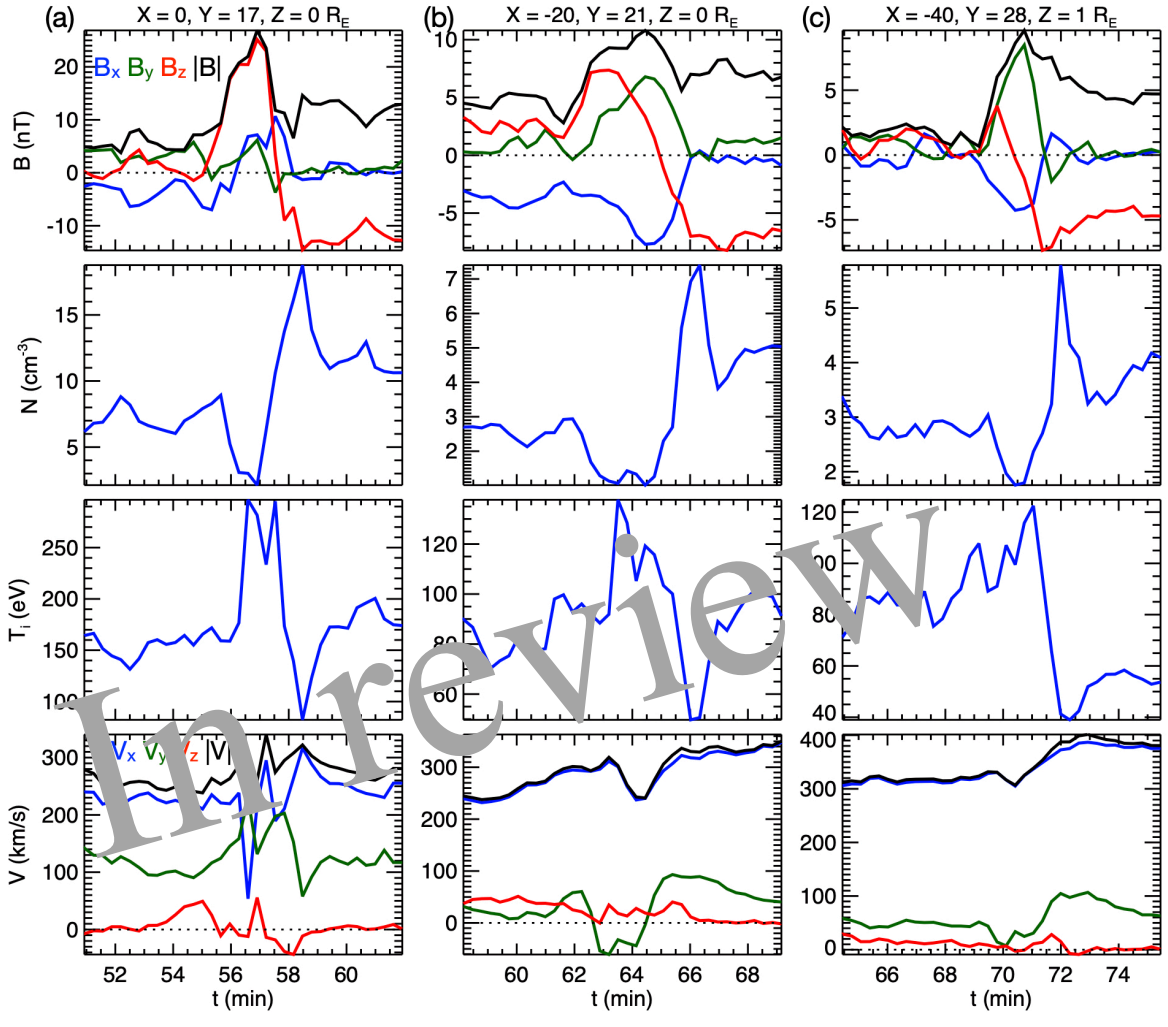

Figure 6. Temporal profiles at (a) X = 0, Y = 17, and Z = 0 R_E, (b) X = –20, Y = 22, and Z = 0 R_E, and (c) X = –40, Y = 28, and Z =1 R_E. From top to bottom: Magnetic field components, number density, ion temperature, and ion bulk flow velocities.

Figure 7.JPEG

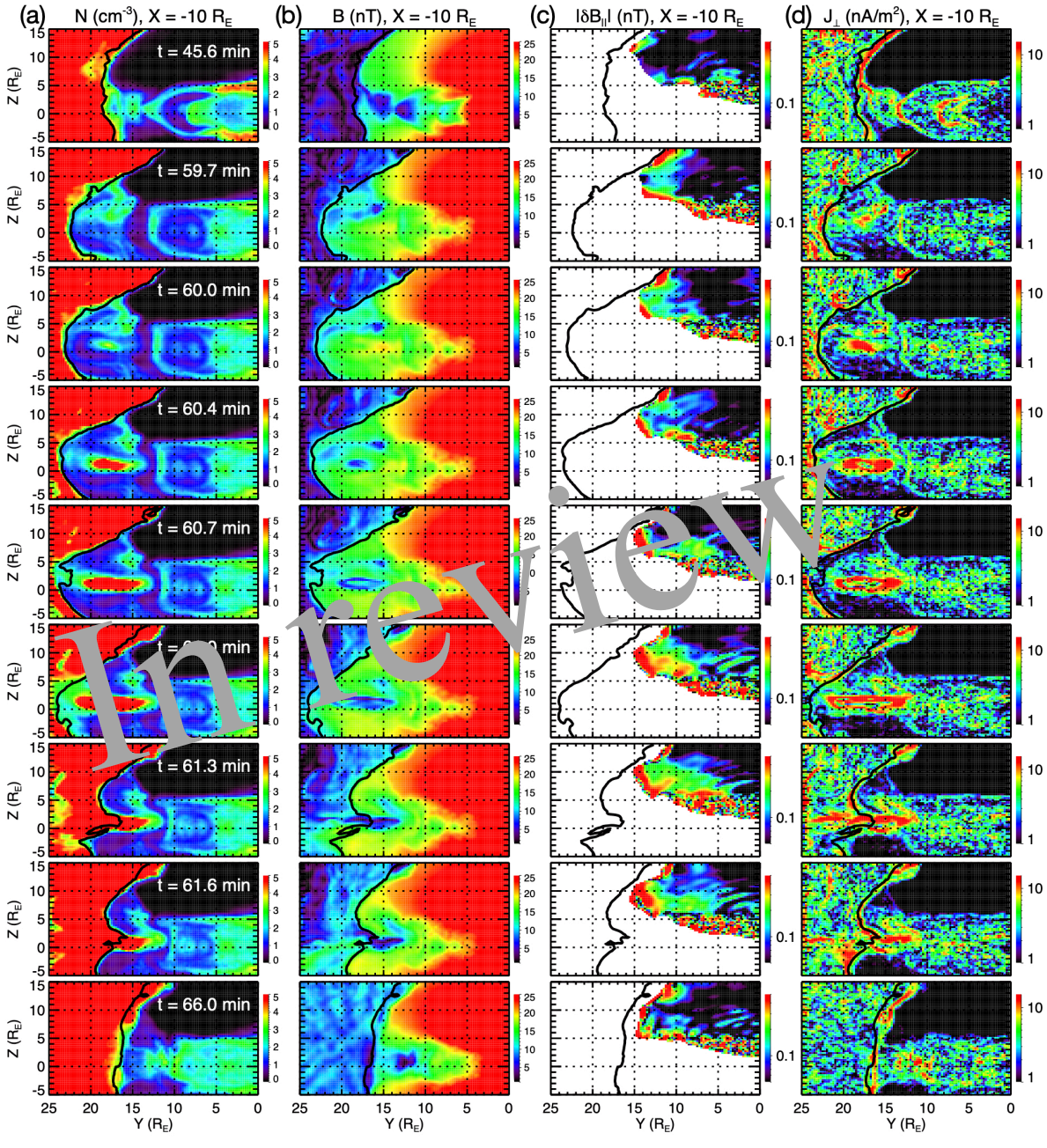

Figure 7. Time sequences of the Y-Z profiles at X = –10 R_E from t = 45.6 to 66 min for (a) number density, (b) magnetic field strength, and (c) the amplitudes of magnetic field perturbations in the parallel direction in the northern lobe where B_x > 15 nT, and (d) perpendicular current density. The black curves indicate approximately the magnetopause.

Figure 8.JPEG

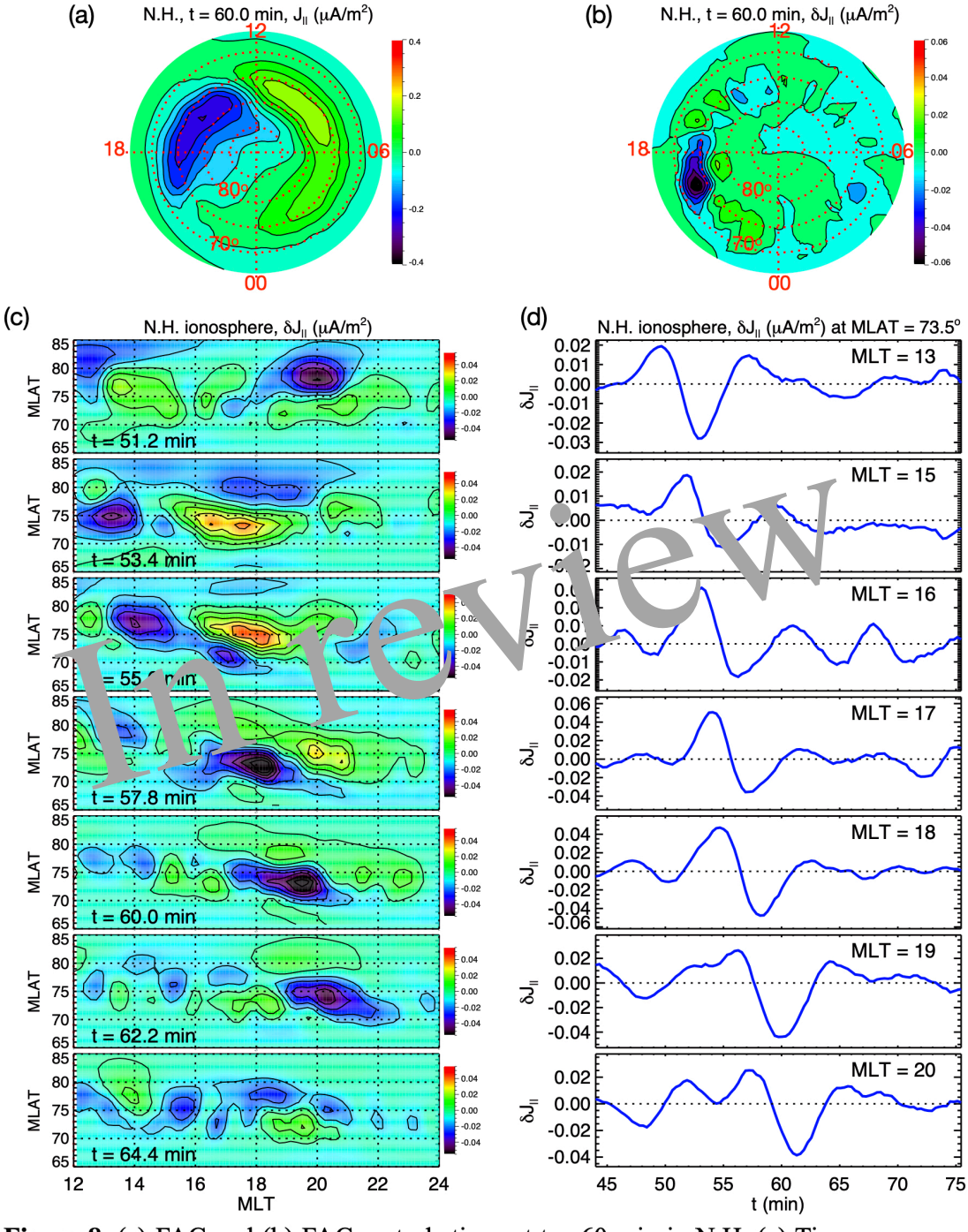

Figure 8. (a) FAC and (b) FAC perturbations at t = 60 min in N.H. (c) Time sequences of the MLAT-MLT distributions for the FAC perturbations in the ionosphere from t = 51.2 to 64.4 min. (b) Time series of the FAC perturbations at different MLTs along MLAT = 73.5°.

Figure 9.JPEG

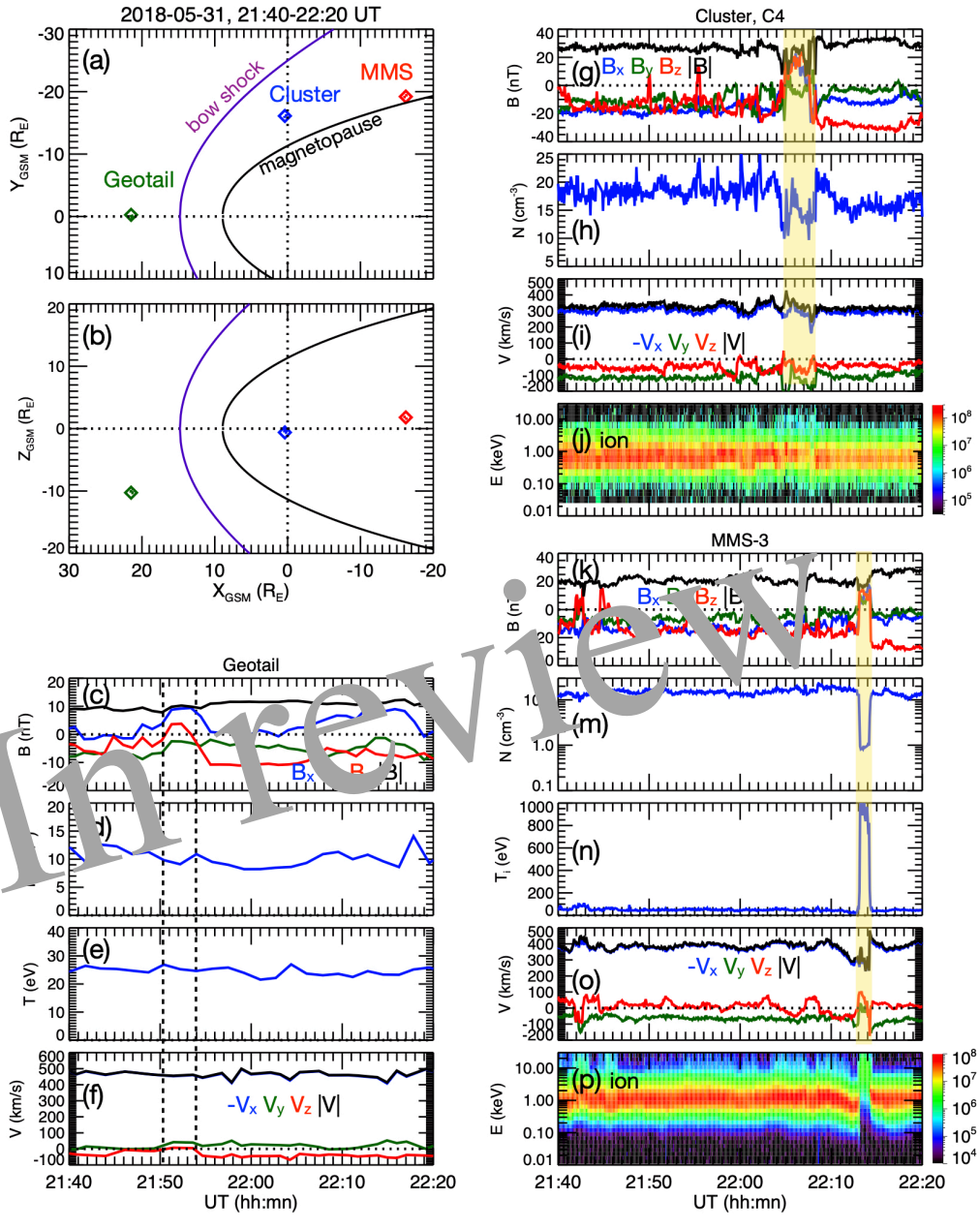

Figure 9. A foreshock transient event on 31 May 2018. The projections of the locations of Geotail, Cluster C4, and MMS-3 on (a) X-Y and (b) X-Z planes. Geotail observations of (c) magnetic field components, (d) number density, (e) ion temperature, and (f) ion bulk flow velocities. The two vertical dashed lines indicate the two discontinuities. Cluster observations of (g) magnetic field components, (h) number density, (i) ion bulk flow velocities, and (j) ion energy flux (eV/(s-sr-cm^2-eV)). The yellow region indicates the magnetosheath perturbation. MMS observations of (k) magnetic field components, (m) number density, (n) ion temperature, (o) ion bulk flow velocities, and (p) ion energy fluxes (eV/(s-sr-cm^2-eV)). The yellow region indicates the magnetosphere.

Figure 10.JPEG

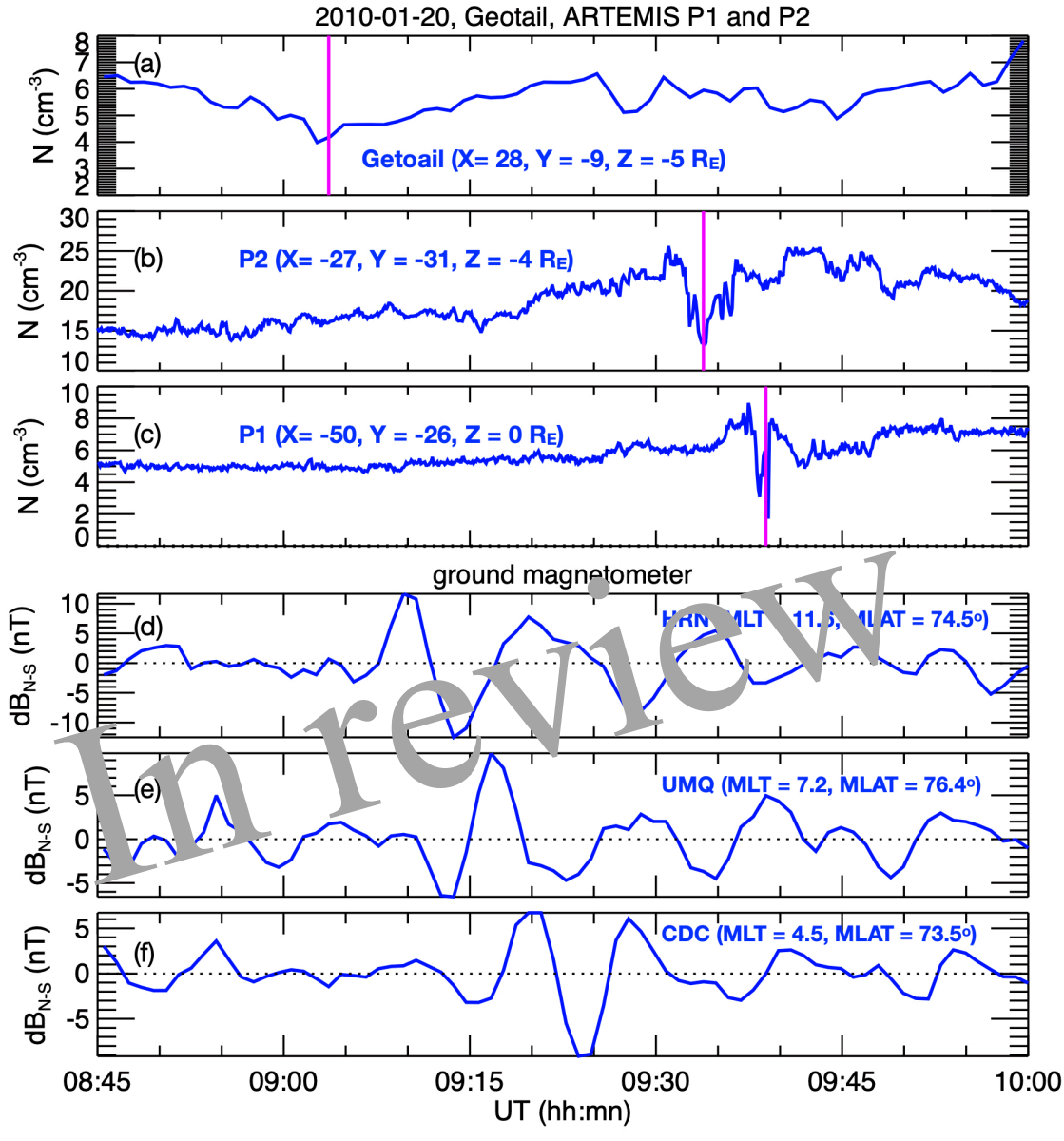

Figure 10. A foreshock transient event on 20 January 2010. The number density observed by (a) Geotail, (b) ARTEMIS P2, and (c) AREMIS P1. The vertical magenta line indicates the time when the IMF discontinuity was observed. The ground magnetic field perturbations (perturbations from 10-min running averages) in the north-south direction observed at (d) HRN, (e) UMQ, and (f) CDC stations.